

High resolution imaging with differential infrared absorption micro-spectroscopy

Isabel Pita,^{1,3} Nordine Hendaoui,^{2,3} Ning Liu,¹ Mahendar Kumbham,¹
Syed A. M. Tofail,¹ André Peremans,^{2,4} and Christophe Silien^{1,*}

¹Department of Physics and Energy, and Materials and Surface Science Institute, University of Limerick, Ireland

²Centre de Recherche en Physique de la Matière et des Rayonnements, Facultés Universitaires Notre Dame de la Paix, Namur, Belgium

³These authors contributed equally to this work

⁴andre.peremans@fundp.ac.be

*christophe.silien@ul.ie

Abstract: Although confocal infrared (IR) absorption micro-spectroscopy is well established for far-field chemical imaging, its scope remains restricted since diffraction limits the spatial resolution to values a little above half the radiation wavelength. Yet, the successful implementations of below-the-diffraction limit far-field fluorescence microscopies using saturated irradiation patterns for example for stimulated-emission depletion and saturated structured-illumination suggest the possibility of using a similar optical patterning strategy for infrared absorption mapping at high resolution. Simulations are used to show that the simple mapping of the difference in transmitted/reflected IR energy between a saturated vortex-shaped beam and a Gaussian reference with a confocal microscope affords the generation of high-resolution vibrational absorption images. On the basis of experimentally relevant parameters, the simulations of the differential absorption scheme reveal a spatial resolution better than a tenth of the wavelength for incident energies about a decade above the saturation threshold. The saturated structured illumination concepts are thus expected to be compatible with the establishment of point-like point-spread functions for measuring the absorbance of samples with a scanning confocal microscope recording the differential transmission/reflection.

©2013 Optical Society of America

OCIS codes: (170.0180) Microscopy; (300.1030) Absorption; (300.6340) Spectroscopy, infrared; (300.6360) Spectroscopy, laser; (300.6390) Spectroscopy, molecular.

References and links

1. W. Min, C. W. Freudiger, S. Lu, and X. S. Xie, "Coherent nonlinear optical imaging: beyond fluorescence microscopy," *Annu. Rev. Phys. Chem.* **62**(1), 507–530 (2011).
2. A. Volkmer, L. D. Book, and X. S. Xie, "Time-resolved coherent anti-Stokes Raman scattering microscopy: imaging based on Raman free induction decay," *Appl. Phys. Lett.* **80**(9), 1505–1507 (2002).
3. M. Jurna, J. P. Korterik, C. Otto, J. L. Herek, and H. L. Offerhaus, "Background free CARS imaging by phase sensitive heterodyne CARS," *Opt. Express* **16**(20), 15863–15869 (2008).
4. C. L. Evans, E. O. Potma, M. Puoris'haag, D. Côté, C. P. Lin, and X. S. Xie, "Chemical imaging of tissue in vivo with video-rate coherent anti-Stokes Raman scattering microscopy," *Proc. Natl. Acad. Sci. U.S.A.* **102**(46), 16807–16812 (2005).
5. M. Balu, G. Liu, Z. Chen, B. J. Tromberg, and E. O. Potma, "Fiber delivered probe for efficient CARS imaging of tissues," *Opt. Express* **18**(3), 2380–2388 (2010).
6. I. Toytman, K. Cohn, T. Smith, D. Simanovskii, and D. Palanker, "Non-scanning CARS microscopy using wide-field geometry," *Proc. SPIE* **6442**, 64420D, 64420D-7 (2007).
7. C. W. Freudiger, W. Min, B. G. Saar, S. Lu, G. R. Holtom, C. He, J. C. Tsai, J. X. Kang, and X. S. Xie, "Label-free biomedical imaging with high sensitivity by stimulated Raman scattering microscopy," *Science* **322**(5909), 1857–1861 (2008).
8. G. Romero, E. Rojas, I. Estrela-Lopis, E. Donath, and S. E. Moya, "Spontaneous confocal Raman microscopy: a tool to study the uptake of nanoparticles and carbon nanotubes into cells," *Nanoscale Res. Lett.* **6**(1), 429 (2011).
9. H. Kim, C. A. Michaels, G. W. Bryant, and S. J. Stranick, "Comparison of the sensitivity and image contrast in spontaneous Raman and coherent Stokes Raman scattering microscopy of geometry-controlled samples," *J. Biomed. Opt.* **16**(2), 021107 (2011).

10. G. L. Carr, "Resolution limits for infrared microspectroscopy explored with synchrotron radiation," *Rev. Sci. Instrum.* **72**(3), 1613–1619 (2001).
11. D. McNaughton, "Synchrotron infrared spectroscopy in biology and biochemistry," *Aust. Biochem.* **36**, 55–58 (2005).
12. H.-Y. N. Holman, R. Miles, Z. Hao, E. Wozei, L. M. Anderson, and H. Yang, "Real-time chemical imaging of bacterial activity in biofilms using open-channel microfluidics and synchrotron FTIR spectromicroscopy," *Anal. Chem.* **81**(20), 8564–8570 (2009).
13. E. Stavitski, M. H. F. Kox, I. Swart, F. M. F. de Groot, and B. M. Weckhuysen, "In situ synchrotron-based IR microspectroscopy to study catalytic reactions in zeolite crystals," *Angew. Chem. Int. Ed. Engl.* **47**(19), 3543–3547 (2008).
14. P. Dumas, G. D. Sockalingum, and J. Sulé-Suso, "Adding synchrotron radiation to infrared microspectroscopy: what's new in biomedical applications?" *Trends Biotechnol.* **25**(1), 40–44 (2007).
15. E. Levenson, P. Lerch, and M. C. Martin, "Spatial resolution limits for synchrotron-based infrared spectromicroscopy," *Infra. Phys. Tech.* **51**(5), 413–416 (2008).
16. P. Dumas and L. Miller, "The use of synchrotron infrared microspectroscopy in biological and biomedical investigations," *Vib. Spectrosc.* **32**(1), 3–21 (2003).
17. H.-Y. N. Holman, H. A. Bechtel, Z. Hao, and M. C. Martin, "Synchrotron IR spectromicroscopy: chemistry of living cells," *Anal. Chem.* **82**(21), 8757–8765 (2010).
18. G. Ellis, G. Santoro, M. A. Gómez, and C. Marco, "Synchrotron IR microspectroscopy: opportunities in polymer science," *IOP Conf. Ser.: Mater. Sci. Eng.* **14**, 012019 (2010).
19. M. J. Nasse, M. J. Walsh, E. C. Mattson, R. Reininger, A. Kajdacsy-Balla, V. Macias, R. Bhargava, and C. J. Hirschmugl, "High-resolution Fourier-transform infrared chemical imaging with multiple synchrotron beams," *Nat. Methods* **8**(5), 413–416 (2011).
20. G. L. Carr and G. P. Williams, "Infrared microspectroscopy with synchrotron radiation," *Proc. SPIE* **3153**, 51–58 (1997).
21. F. Huth, M. Schnell, J. Wittborn, N. Ocelic, and R. Hillenbrand, "Infrared-spectroscopic nanoimaging with a thermal source," *Nat. Mater.* **10**(5), 352–356 (2011).
22. F. Lu and M. A. Belkin, "Infrared absorption nano-spectroscopy using sample photoexpansion induced by tunable quantum cascade lasers," *Opt. Express* **19**(21), 19942–19947 (2011).
23. B. Knoll and F. Keilmann, "Near-field probing of vibrational absorption for chemical microscopy," *Nature* **399**(6732), 134–137 (1999).
24. S. W. Hell, M. Dyba, and S. Jakobs, "Concepts for nanoscale resolution in fluorescence microscopy," *Curr. Opin. Neurobiol.* **14**(5), 599–609 (2004).
25. S. W. Hell and J. Wichmann, "Breaking the diffraction resolution limit by stimulated emission: stimulated-emission-depletion fluorescence microscopy," *Opt. Lett.* **19**(11), 780–782 (1994).
26. T. A. Klar, S. Jakobs, M. Dyba, A. Egner, and S. W. Hell, "Fluorescence microscopy with diffraction resolution barrier broken by stimulated emission," *Proc. Natl. Acad. Sci. U.S.A.* **97**(15), 8206–8210 (2000).
27. E. Rittweger, K. Y. Han, S. E. Irvine, C. Eggeling, and S. W. Hell, "STED microscopy reveals crystal colour centres with nanometric resolution," *Nat. Photonics* **3**(3), 144–147 (2009).
28. D. Wildanger, R. Medda, L. Kastrop, and S. W. Hell, "A compact STED microscope providing 3D nanoscale resolution," *J. Microsc.* **236**(1), 35–43 (2009).
29. E. Rittweger, D. Wildanger, and S. W. Hell, "Far-field fluorescence nanoscopy of diamond color centers by ground state depletion," *Europhys. Lett.* **86**(1), 14001 (2009).
30. S. W. Hell and M. Kroug, "Ground-state-depletion fluorescence microscopy: a concept for breaking the diffraction resolution limit," *Appl. Phys. B* **60**(5), 495–497 (1995).
31. S. Bretschneider, C. Eggeling, and S. W. Hell, "Breaking the diffraction barrier in fluorescence microscopy by optical shelving," *Phys. Rev. Lett.* **98**(21), 218103 (2007).
32. J. Kwon, Y. Lim, J. Jung, and S. K. Kim, "New sub-diffraction-limit microscopy technique: dual-point illumination AND-gate microscopy on nanodiamonds (DIAMOND)," *Opt. Express* **20**(12), 13347–13356 (2012).
33. M. G. L. Gustafsson, "Nonlinear structured-illumination microscopy: wide-field fluorescence imaging with theoretically unlimited resolution," *Proc. Natl. Acad. Sci. U.S.A.* **102**(37), 13081–13086 (2005).
34. E. H. Rego, L. Shao, J. J. Macklin, L. Winoto, G. A. Johansson, N. Kamps-Hughes, M. W. Davidson, and M. G. L. Gustafsson, "Nonlinear structured-illumination microscopy with a photoswitchable protein reveals cellular structures at 50-nm resolution," *Proc. Natl. Acad. Sci. U.S.A.* **109**(3), E135–E143 (2012).
35. M. J. Rust, M. Bates, and X. Zhuang, "Sub-diffraction-limit imaging by stochastic optical reconstruction microscopy (STORM)," *Nat. Methods* **3**(10), 793–796 (2006).
36. B. Huang, W. Wang, M. Bates, and X. Zhuang, "Three-dimensional super-resolution imaging by stochastic optical reconstruction microscopy," *Science* **319**(5864), 810–813 (2008).
37. R. Heintzmann, V. Sarafis, P. Munroe, J. Nailon, Q. S. Hanley, and T. M. Jovin, "Resolution enhancement by subtraction of confocal signals taken at different pinhole sizes," *Micron* **34**(6-7), 293–300 (2003).
38. O. Schwartz and D. Oron, "Using variable pupil filters to optimize the resolution in multiphoton and saturable fluorescence confocal microscopy," *Opt. Lett.* **34**(4), 464–466 (2009).
39. Y. Wang, C. Kuang, Z. Gu, and X. Liu, "Image subtraction method for improving lateral resolution and SNR in confocal microscopy," *Opt. Laser Technol.* **48**, 489–494 (2013).
40. O. Haeblerlé and B. Simon, "Saturated structured confocal microscopy with theoretically unlimited resolution," *Opt. Commun.* **282**(18), 3657–3664 (2009).

41. C. Kuang, S. Li, W. Liu, X. Hao, Z. Gu, Y. Wang, J. Ge, H. Li, and X. Liu, "Breaking the Diffraction Barrier Using Fluorescence Emission Difference Microscopy," *Sci. Rep.* **3**, 1441 (2013).
42. W. P. Beeker, P. Gross, C. J. Lee, C. Cleff, H. L. Offerhaus, C. Fallnich, J. L. Herek, and K.-J. Boller, "A route to sub-diffraction-limited CARS Microscopy," *Opt. Express* **17**(25), 22632–22638 (2009).
43. W. P. Beeker, C. J. Lee, K.-J. Boller, P. Groß, C. Cleff, C. Fallnich, H. L. Offerhaus, and J. L. Herek, "Spatially dependent Rabi oscillations: an approach to sub-diffraction-limited coherent anti-Stokes Raman-scattering microscopy," *Phys. Rev. A* **81**(1), 012507 (2010).
44. C. Silien, N. Liu, N. Hendaoui, S. A. M. Tofail, and A. Peremans, "A framework for far-field infrared absorption microscopy beyond the diffraction limit," *Opt. Express* **20**(28), 29694–29704 (2012).
45. T. Watanabe, M. Fujii, Y. Watanabe, N. Toyama, and Y. Iketaki, "Generation of a doughnut-shaped beam using a spiral phase plate," *Rev. Sci. Instrum.* **75**(12), 5131–5135 (2004).
46. D. Wildanger, J. Bückers, V. Westphal, S. W. Hell, and L. Kastrup, "A STED microscope aligned by design," *Opt. Express* **17**(18), 16100–16110 (2009).
47. J. Keller, A. Schönle, and S. W. Hell, "Efficient fluorescence inhibition patterns for RESOLFT microscopy," *Opt. Express* **15**(6), 3361–3371 (2007).
48. X. Hao, C. Kuang, T. Wang, and X. Liu, "Effects of polarization on the de-excitation dark focal spot in STED microscopy," *J. Opt.* **12**(11), 115707 (2010).
49. W. Demtroder, *Laser spectroscopy: basic concepts and instrumentation* (Springer-Verlag, 2003).
50. D. A. Guzonas, M. L. Hair, and C. P. Tripp, "Infrared spectra of monolayers adsorbed on mica," *Appl. Spectrosc.* **44**(2), 290–293 (1990).
51. A. L. Harris, L. Rothberg, L. Dhar, N. J. Levinos, and L. H. Dubois, "Vibrational energy relaxation of a polyatomic adsorbate on a metal surface: methyl thiolate (CH₃S) on Ag(111)," *J. Chem. Phys.* **94**(4), 2438 (1991).
52. H. J. Bakker, P. C. M. Planken, and A. Lagendijk, "Ultrafast vibrational dynamics of small organic molecules in solution," *J. Chem. Phys.* **94**(9), 6007–6013 (1991).
53. R. P. Chin, X. Blase, Y. R. Shen, and S. G. Louie, "Anharmonicity and lifetime of the CH stretch mode on diamond H/C(111)-(1×1)," *Europhys. Lett.* **30**(7), 399–404 (1995).
54. J. Löbau and A. Laubereau, "Surface studies using non-linear spectroscopy with tunable picosecond pulses," *Proc. SPIE* **3683**, 96–107 (1998).
55. G. Seifert, M. Bartel, and H. Graener, "Relaxation of the CH₂ stretching modes of liquid dihalomethanes," *Open Phys. Chem. J.* **2**(1), 22–28 (2008).
56. W. Kaiser, A. Fendt, W. Kranitzky, and A. Laubereau, "Infrared picosecond pulses and applications," *Philos. Trans. Roy. Soc. A* **298**(1439), 267–271 (1980).
57. L. K. Iwaki and D. D. Dlott, "Ultrafast vibrational energy redistribution within C-H and O-H stretching modes of liquid methanol," *Chem. Phys. Lett.* **321**(5-6), 419–425 (2000).
58. M. Saß, M. Lettenberger, and A. Laubereau, "Orientation and vibrational relaxation of acetonitrile at a liquid:solid interface, observed by sum-frequency spectroscopy," *Chem. Phys. Lett.* **356**(3-4), 284–290 (2002).
59. H. J. Bakker, P. C. M. Planken, and A. Lagendijk, "Ultrafast vibrational dynamics of small organic molecules in solution," *J. Chem. Phys.* **94**(9), 6007–6013 (1991).
60. I. Hartl and W. Zinth, "A novel spectrometer system for the investigation of vibrational energy relaxation with sub-picosecond time resolution," *Opt. Commun.* **160**(1-3), 184–190 (1999).
61. M. G. L. Gustafsson, "Surpassing the lateral resolution limit by a factor of two using structured illumination microscopy," *J. Microsc.* **198**(2), 82–87 (2000).
62. L. Novotny and B. Hecht, *Principles of nano-optics* (Cambridge University Press, 2006).
63. B. A. Nechay, U. Siegner, M. Achermann, H. Bielefeldt, and U. Keller, "Femtosecond pump-probe near-field optical microscopy," *Rev. Sci. Instrum.* **70**(6), 2758–2764 (1999).
64. F. K. Tittel, D. Richter, and A. Fried, "Mid-Infrared Laser Applications in Spectroscopy," in *Solid-State Mid-Infrared Laser Sources*, I. T. Sorokina and K. L. Vodopyanov, eds, *Topics Appl. Phys.* **89**, 445-516 (2003).

1. Introduction

The increasing demand for structural imaging and spectral analysis of biological and non-biological specimens at sub-cellular, sub-micron or nanometer resolution motivates the development of high resolution micro-spectroscopy techniques. Among those, optical vibrational spectroscopies such as coherent anti-Stokes Raman spectroscopy (CARS) [1–6], stimulated Raman scattering [7], spontaneous Raman [8,9], and Fourier-transform infrared absorption spectroscopy (IRAS) [10–20] reveal molecular fingerprints because the vibrational modes of molecules are dependent on chemical bonds and local molecular arrangements. Thus label-free imaging is readily achieved by mapping spatially localized spectra.

However, in the far-field, diffraction limits the resolution to values between λ and $\lambda/2$, where λ is the wavelength of the radiation used for imaging, and imposes thus a severe limitation in resolution especially for IRAS since in the mid-infrared the wavelengths span from 2 to 20 μm . Moreover, only synchrotrons provide broadband mid-IR sources of sufficient brightness to map efficiently the IR absorption at the diffraction limit using

confocal microscopes, and IRAS table-top microscopes using thermal sources must be used at degraded resolution to achieve a realistic signal-to-noise ratio (SNR) [10–20]. For a given wavelength, pulsed tunable IR laser sources match or exceed the brightness of synchrotron and can in principle be readily used for diffraction limited IRAS, although one trade-off is that only a single wavelength can be probed at a time. Today IRAS imaging with spatial resolution beyond the diffraction limit is achieved using near-field approaches (50-100 nm) with either broadband thermal sources or IR lasers [21–23]. However, these techniques are limited to probing surfaces since they involve the scanning of the samples by a material probe. Developing far-field and table-top approaches for high resolution IRAS imaging that can overcome the above limitations remains thus highly desirable.

Pushed by the strong demand in life science, several schemes for achieving sub-diffraction and, as a matter of fact, true nanoscale imaging, have been successfully developed with far-field fluorescence microscopy [24]. These include reversible optical fluorescence transition (RESOLFT) microscopies such as for example stimulated emission depletion (STED) microscopy [25–32], non-linear saturated structured illumination microscopy (SSIM) [33,34], and single molecule localization microscopies such as stochastic optical reconstruction microscopy (STORM) [35,36]. Several image subtraction methods have also been developed to improve the lateral resolution of fluorescence confocal microscopy, using different detection pinhole geometry [37–39] or vortex-shaped illumination [40,41]. However, all these methods generally require the introduction of fluorescent markers in the samples which are the species that is truly measured in the samples.

Chemically sensitive label-free imaging with sub-diffraction resolution is on the other hand deemed possible based on the vibrational spectroscopies CARS [42,43] and IRAS [44]. It is envisaged to control the spatial extension of the CARS emission using a vortex-shaped beam to suppress the vibrational Raman coherence through an incoherent process involving the excitation of a neighboring vibration or to periodically deplete the ground-state through Rabi oscillations. The scheme for IRAS involves a vortex-shaped IR pulse for saturating the vibrational mode of interest and subsequent probing with a second, delayed IR pulse [44]. The expected improvement in spatial resolution is down to ca. 65 nm for CARS [43], and down to about $\lambda/13$ for IRAS using the vibrational depletion pump-probe scheme [44]. In both cases these values would represent a breakthrough.

Except for the single molecule localization techniques, the microscopies above achieve resolutions below the diffraction limit because of the spatial structuring of an incident radiation that exhibits either a single circular node (vortex) or a sinusoidal intensity profile, and that is sufficiently intense for saturating one optical process involved in the imaging. Thus, although more than one radiation is used depending on the optical information that is measured, only one is responsible for the resolution. For IRAS, and by extension for any optical absorption technique, we rationalize that only this one spatially structured radiation is required since the absorption can also be detected as a loss in its energy. This hypothesis is discussed and elaborated in this paper on the basis of simulations of the absorption of spatially defined intense IR beams in a mock organic sample. A single radiation scheme would indeed be experimentally attractive since for example, with respect to the vibrational depletion pump-probe scheme proposed earlier [44], pulse duration, pump-probe delay, and probe pump separation at the detector are then not relevant.

The simulations illustrate that a sensitive scanning scheme is possible by measuring with a confocal microscope the difference in transmitted/reflected energy between a vortex-shaped radiation and a reference taken here as Gaussian. The difference is proportional to the local absorbance. The spatial resolution is found to be down to less than $\lambda/10$ for a vortex about a decade above the saturation threshold. Although the sensitivity is a little less than the previously reported vibrational-depletion pump-probe scheme [44] for IRAS, the simulations reveal that, for the CH_2 stretches, 300 nm large mock organic alkane bulk specimens lead to a differential signal about 0.05% of the full transmitted/reflected vortex intensity, a value that is well within measurable range.

2. Scheme for differential absorption

We consider the irradiation of a sample incorporating two-level oscillators with an IR beam tuned to the wavelength of the vibrational transition, and with a pulsed temporal structure that, from an experimental point of view, will be necessary to achieve saturation of the transition, but that will not be required otherwise. We further consider that the IR beam is focused on the sample so that it exhibits a node along the optical axis, which is readily made experimentally with a vortex phase plate [45–48]. A vortex absorption point-spread function (PSF) is then defined by

$$PSF_{vortex} \propto \Sigma_{0,vortex}(x, y) - \Sigma_{vortex}(x, y) \quad (1)$$

where $\Sigma_{vortex}(x, y)$ is the energy of the vortex pulse after absorption in the sample at the coordinates (x, y) defined in the sample plane, and where the indice 0 denotes the same quantity measured in the absence of absorption. The shape of the vortex PSF is reminiscent of the vortex geometry [Fig. 1]. However, because the sample will not absorb more photons than necessary to achieve saturation, that is, to excite half the local population of oscillators, the vortex PSF will plateau where the intensity on the sample is larger than the saturation threshold and will thus exhibit a node of width narrowing with the vortex pulse energy, and, as demonstrated experimentally with RESOLFT microscopy schemes, the width of the node can be much smaller than the diffraction limit [26–29,31,46].

The recovery of an absorption image confined to the region of that sub-diffraction node can be envisaged by subtraction from an image of reference defined with a PSF that ideally matches with that of the vortex one, except at the center where the node is absent. In an experiment, such a reference PSF can be readily approached by a Gaussian whose central part will be of uniform height for intensity above the saturation threshold. The absorption microscopy PSF for the Gaussian may be written as

$$PSF_{Gauss} \propto \Sigma_{0,Gauss}(x, y) - \Sigma_{Gauss}(x, y) \quad (2)$$

where $\Sigma_{Gauss}(x, y)$ is the energy of the Gaussian pulse after absorption in the sample, and where the indice 0 denotes the same quantity in the absence of absorption. The difference Δ between the two PSFs

$$\Delta = PSF_{Gauss} - PSF_{vortex} \quad (3)$$

gives a spatial profile illustrated in Fig. 1(c), and one readily sees that a desirably peak-shaped differential IR (DIR) PSF will thus be achieved by directly measuring the difference between vortex and Gaussian beams after absorption in the sample:

$$PSF_{DIR} \propto \Sigma_{vortex}(x, y) - \Sigma_{Gauss}(x, y) \propto \Delta(x, y) - C \quad (4)$$

where C is a constant background for all (x, y) coordinates and scales simply with the difference in measured energy between vortex and Gaussian pulses in the absence of absorption.

Equation (4) suggests an experimental scheme to realize the method in which periodically alternating series of vortex and Gaussian pulses are focused onto the sample. The integrated intensity measured after absorption in the sample will then exhibit a component of the same period. The latter component is indeed proportional to the desired differential absorption signal and can be readily measured by synchronous detection, for example. The differential absorption image is then generated by mapping this signal, by varying the sample position in the beams. Noteworthy, although the differential PSF exhibits a central peak that clearly stands out of the background, an imperfect match between the vortex and reference spatial profiles away from the central axis will generate concentric rings around the peak [see side lobes in Fig. 1(d)], which are obviously undesirable artifacts. The precise shape of the

reference beam, taken here as Gaussian, is thus crucial. However, as it will be discussed below, the use of a confocal arrangement for collecting the beam drastically improves the PSF by strongly reducing these side-lobes.

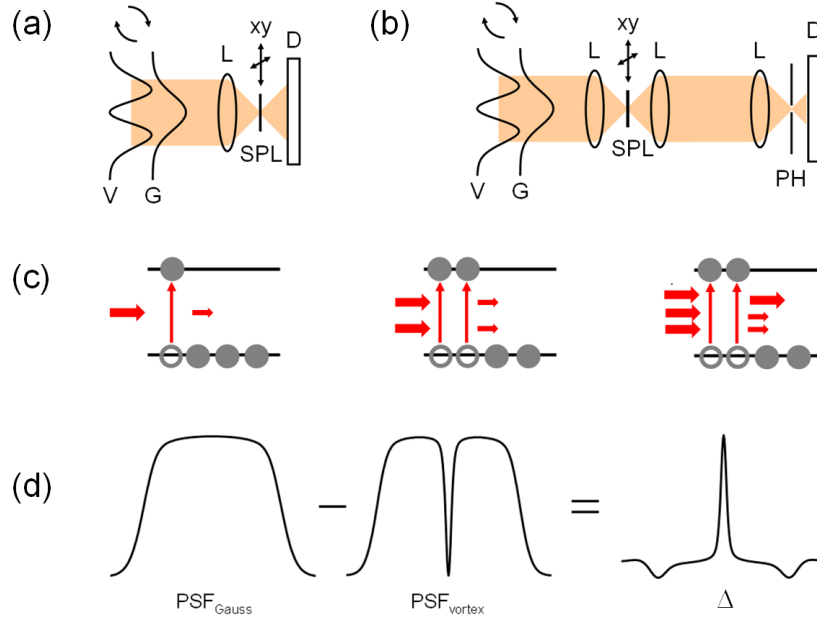


Fig. 1. (a) Differential absorption microscopy scheme where reference Gaussian (G) and vortex-shaped (V) pulses are focused by a lens (L) alternatively on the sample (SPL) and where the transmitted intensity is integrated by a detector (D). A scanner is used for producing images (xy). (b) Same as (a) but with confocal spatial filtering of the transmitted beam using a pinhole (PH). (c) Illustration of the transmission and change in population of a system of two-level oscillators for increasing incident intensity. (d) Difference Δ between vortex and reference PSF.

3. Model

The algorithm and Matlab™ scripts used here to model the differential absorption scheme have been adapted from those reported in [44]. The scripts consider that the measurements are made in transmission, since the temporal evolution of the intensity is then simpler to compute. Noteworthy, the differential scheme is expected to perform the same in reflection, which will be simpler to implement experimentally as only one objective needs then to be aligned. The sample is modeled in space as an ensemble of voxels containing each a collection of independent oscillators and, for each sample voxel, the change in intensity due to stimulated absorption/emission [49], along the coordinate z defined as the axis of propagation of the light pulses, normal to the sample surface, is inferred from

$$\frac{dI}{dz} = \frac{hc}{\lambda} k(\mathbf{r}) \rho(\mathbf{r}) \Delta N(\mathbf{r}, t) I(\mathbf{r}, t) \quad (5)$$

where k is the stimulated emission/absorption Einstein coefficient, ρ is the density of oscillators, ΔN is the difference in relative population density between the fundamental and excited vibrational state, $I(\mathbf{r}, t)$ is the local intensity at a given time t and sample position $\mathbf{r} = (x, y, z)$, with (x, y) the coordinates in the sample plane set as normal to the direction of propagation of the light, and h and c are respectively the Planck constant and the speed of light in vacuum. ΔN is determined by

$$\frac{dN}{dt} = -\Gamma(\mathbf{r}) N(\mathbf{r}) - k(\mathbf{r}) \Delta N(\mathbf{r}, t) I(\mathbf{r}, t) \quad (6)$$

where Γ is the spontaneous de-excitation rate, and N the relative population density of excited oscillators at a given position in the sample.

The system of Eq. (5) and Eq. (6) is readily solved using the backward Euler approach and independently for each set of (x, y) coordinates. The solution is found by iteration with the boundary conditions $N(\mathbf{r}, t_0) = 0$, where t_0 is a reference time before irradiation of the sample. $I(x, y, z_0, t) = 0$ describes the spatial and temporal structures of the vortex and reference pulses impinging the sample at z_0 :

$$I_{\text{vortex}}(r, t) = I_{0, \text{vortex}} r^2 e^{-r^2/w_0^2} e^{-t^2/\tau_0^2} \quad (7)$$

and

$$I_{\text{Gauss}}(r, t) = I_{0, \text{Gauss}} e^{-r^2/w_0^2} e^{-t^2/\tau_0^2} \quad (8),$$

where r and θ are the polar coordinates in the plane normal to the direction of propagation, and where $I_{0, \text{vortex}}$ and $I_{0, \text{Gauss}}$ are constants adjusted to reproduce the desired pulse energies. The pulse duration are then given by $2\sqrt{\ln(2)} \tau_0$ and the spatial extension of the pulses on the sample are defined by the waist w_0 , which corresponds to a full width at half maximum (FWHM) of $2\sqrt{\ln(2)} w_0$ for the Gaussian profile and a FWHM ca. 1.8 times larger for the vortex profile.

The energy Σ of the pulses after absorption in the sample is computed by integrating the intensity in the sample plane (x, y) and over time, at the coordinate z exceeding the sample thickness, for a given relative position of the sample in the beams. IR absorption and differential IR absorption images are then created by repeating the calculations whilst scanning the relative sample position. In line with Eq. (1), Eq. (2), and Eq. (4), the differential IR absorption is defined by

$$DIR(\%) = \frac{\Sigma_{\text{vortex}} - \Sigma_{\text{Gauss}}}{\Sigma_{0, \text{vortex}}} \times 100 \quad (9),$$

where the normalization to the incident energy $\Sigma_{0, \text{vortex}}$ affords an assessment of the sensitivity of the method.

In line with [44], λ , k , ρ , and Γ are set to $3.5 \mu\text{m}$, $1.4 \text{ nm}^2 \cdot \text{fJ}^{-1}$, 31.5 nm^{-3} , and 0.1 ps^{-1} which, for a thickness of 2.0 nm , reproduce the properties of a monolayer of octadecyltrichlorosilane on a dielectric substrate for which experimental measurements reveals ca. 0.5% of absorption by the CH_2 stretch modes [50]. The decay rate Γ was set at 0.1 ps^{-1} because experimental measurements of the lifetime of CH stretch modes revealed values spanning from as little as a few picoseconds up to several hundreds of picoseconds [51–60].

Aiming to a realistic prediction of the differential IR absorption microscopy performances, the FWHM of the Gaussians was set to values that are no smaller than those expected with an objective of numerical aperture (NA) 0.85, corresponding to commercially available aspherical lenses at $3.5 \mu\text{m}$. At the diffraction limit, experiments have verified that an objective with NA 0.7 focuses a Gaussian beam with λ at $3.5 \mu\text{m}$ into a spot of FWHM ca. $2.3 \mu\text{m}$ [10] and thus a waist of ca. $1.4 \mu\text{m}$ (FWHM of ca. $1.9 \mu\text{m}$) is thus readily expected for a NA of 0.85 by interpolation. The waist w_0 of the vortex was adjusted to that value

producing a pattern where the distance between two maxima along the diameter of the vortex spot is $2.2\ \mu\text{m}$, in agreement with the value that we have found using the vectorial diffraction theory detailed in [48]. For the Gaussian reference, larger waists were also used to facilitate the compensation of the naturally broader vortex. Noteworthy, when the confocal spatial filtering is taken into account the compensation is facilitated and is adequate also when using Gaussian waist set to the diffraction limit. The pulse duration was arbitrarily set at $1.0\ \text{ps}$, although larger values may also be of experimental interest.

4. Results and discussion

The feasibility of the concept is first examined by computing the differential absorption PSF associated with the CH_2 stretch vibrational mode at ca. $3.5\ \mu\text{m}$ on a sample defined as a single pixel of mock octadecyltrichlorosilane [Fig. 2]. The dimensions of the pixel are set at $25 \times 25\ \text{nm}^2$, which remains small in comparison to the expected resolution. The vortex and reference pulse energy is the same and is varied from $1\ \text{nJ}$ to $1\ \mu\text{J}$. The reference is set as a Gaussian of waist $1.7\ \mu\text{m}$, a value that was found to minimize the magnitude of uncompensated rings around the central PSF peak, although side lobes remain clearly visible for all the energies [Fig. 2(a)].

The resolution is measured as the FWHM of the central PSF peak and its value is plotted in Fig. 2(b), along with the PSF value at the peak in Fig. 2(c). As expected, the FWHM decreases sharply with the energy of the vortex pulse and down to ca. $270\ \text{nm}$ ($\lambda/13$) for $100\ \text{nJ}$, where the vortex maximum intensity is ca. 10 times above the saturation threshold [44]. This vortex energy of $100\ \text{nJ}$ was previously found to be a realistic optimum with respect to the IR irradiation damage threshold of samples at $3.5\ \mu\text{m}$ [44]. Noteworthy, the FWHM is also reduced to around $1.2\ \mu\text{m}$ for values below the saturation threshold ($1\ \text{nJ}$), which is an effect of structured illumination [61].

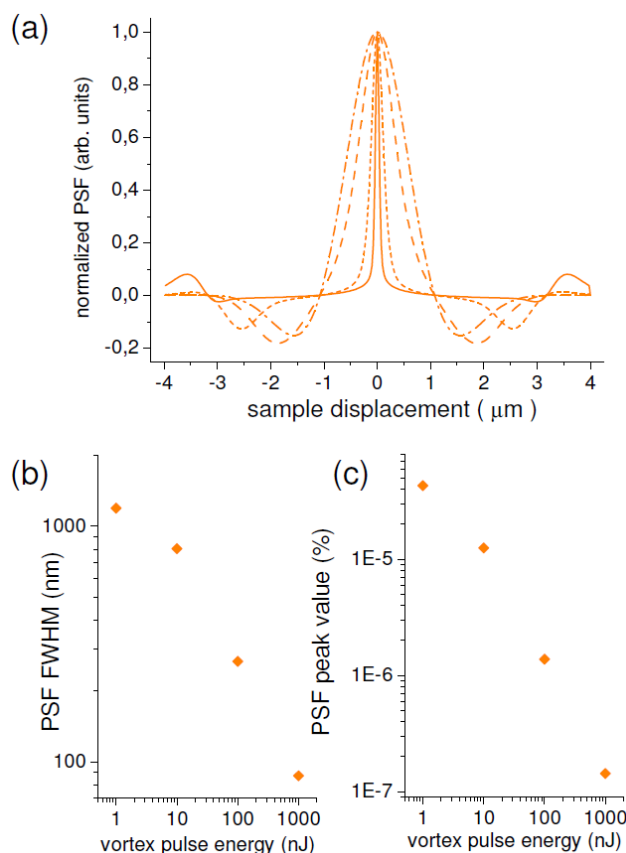


Fig. 2. (a) Differential absorption PSF for vortex energies of 1 μJ (continuous), 100 nJ (shorter dash), 10 nJ (dash), and 1 nJ (dash-dot). The PSF were normalized with their maximum at 1 for clarity. (b) PSF FWHM for the data shown in (a). (c) PSF value at peak for the data shown in (a) without normalization.

The side lobes in the differential absorption PSF seen in Fig. 1(d) and Fig. 2(a), and due to the poor superposition of the vortex and reference away from the optical axis, are very undesirable for high resolution imaging. The side lobes can in principle be reduced by replacing the Gaussian reference by one with a profile that matches better with the vortex. Although possible, this approach is however not straightforward to envisage from an experimental point of view. A better approach for suppressing the side lobes is to make the method less sensitive to these differences between vortex and reference profiles, and it is shown below that a confocal spatial filtering will just do that.

In a confocal microscope, the volume of sample contributing to the detected signal is controlled by the introduction of a pinhole conjugated with a defined sample volume [62]. The confocal spatial filtering effect was introduced in our simulation by weighting the intensities leaving the sample [Eq. (5)] with a Gaussian distribution of diffraction limited FWHM adjusted to a collecting lens of NA 0.85, corresponding to the maximum numerical aperture that is commercially available at 3.5 μm . The differential absorption PSF computed in combination with the confocal spatial filtering are shown in Fig. 3(a) for vortex energies of 10 and 100 nJ. The curves were calculated with the same parameters as those used for the PSF presented in Fig. 2(a) where no spatial filtering of the detected intensity was then introduced. Obviously, in Fig. 3(a), the side lobes are significantly reduced and the PSF are essentially point-like as expected, with a FWHM also marginally reduced.

We further illustrate the differential absorption method by computing IR absorption and differential IR absorption images of a sample made of nine alkane cubes of $300 \times 300 \times 300 \text{ nm}^3$ with the same density of CH_2 as the 2 nm thick octadecyltrichlorosilane film [Fig. 3(b)], and which allow us to assess the merit of the scheme when imaging organic nanoparticles. The pulse energy is set at 100 nJ and the images are computed taking into account of the confocal spatial filtering. The IR absorption image calculated for the reference Gaussian does not reveal any fine feature reminiscent of the nine organic domains, which of course results from the then limited resolution [Fig. 3(c)]. Conversely, for the vortex, the absorption image reveals the nine domains as depressions on a locally varying background consistent with the vortex PSF in Fig. 1(d). For the differential absorption, the domains are resolved as protrusions, marking the increased IR absorption, and the background is now perfectly corrected by the reference [Fig. 3(e)]. Obviously, in an experiment the differential absorption can be recorded with more sensitivity directly by synchronous detection than if both the vortex and Gaussian absorption image are recorded independently.

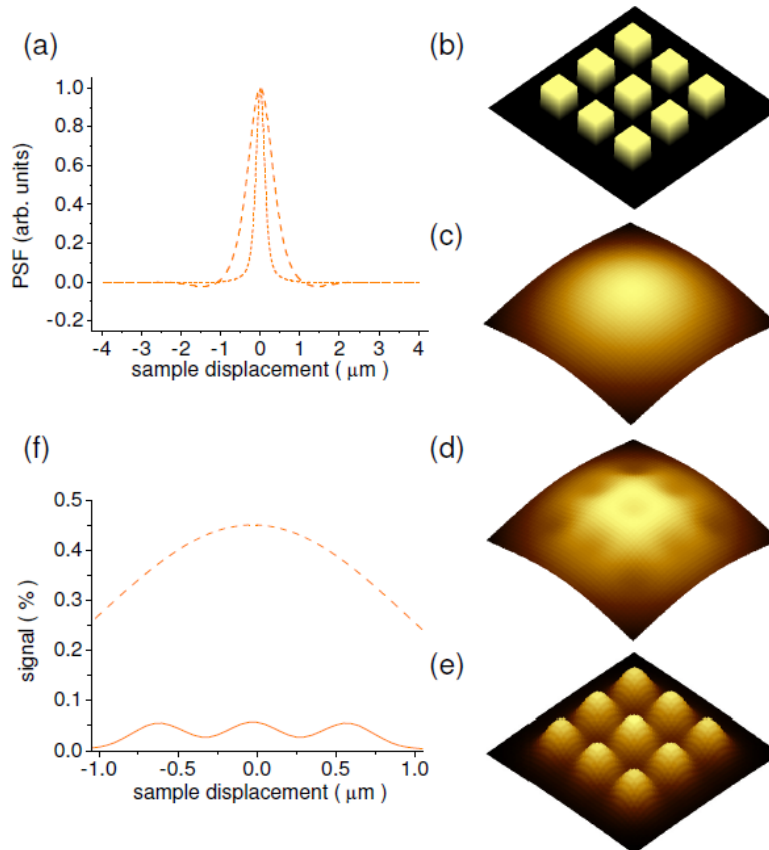


Fig. 3. (a) Differential absorption PSF with confocal spatial filtering for vortex energies of 100 nJ (shorter dash) and 10 nJ (dash) (pixel: $25 \times 25 \text{ nm}^2$). The PSF were normalized with their maximum at 1 for clarity. (b) Sample geometry for an array of nine cubic domains of alkane ($300 \times 300 \times 300 \text{ nm}^3$; 300 nm between domains), (c) corresponding Gaussian reference IR absorption image, (d) vortex IR absorption image, and (e) differential absorption image. (f) Line profiles extracted from the DIR and Gaussian reference images (dash). For (b-f) the pulse energy is 100 nJ and one pixel is $50 \times 50 \text{ nm}^2$.

At the center of a domain the differential signal is 0.05% of the energy reaching the detector [Fig. 3(f)]. The sensitivity of the differential absorption is however expected to be less than the one reported for the vibrational depletion pump-probe scheme, where the

maximum signals for the same sample and with the same vortex at 100 nJ are expected to be at least an order of magnitude higher, for an optimized pump-probe delay [44]. This is because the absorption is here measured superposed to ca. 100 nJ, while for the pump-probe scheme it is superposed to a much weaker probe pulse of ca. 1 nJ. Yet, the SNR required for measuring a cubic 300 nm alkane domains with the differential scheme presented here is thus of the order of 10^{-4} - 10^{-5} (i.e., for a magnitude a decade above noise level). Since earlier works have highlighted that subtraction-based imaging are more noise-sensitive than schemes where imaging is achieved with a single measure [37–41], and that this may impact on the experimental resolution [40], it remains important to compare the SNR requirements of the differential absorption scheme with past experimental achievements in absorption spectroscopy and microscopy. Variations in transmission of the order of 10^{-4} were recorded in a pump-probe absorption microscopy scheme [63] and a SNR of 16:1 rms was achieved when detecting IR absorption in a Fourier transform setup with a reference beam 10^4 more intense than the signal beam [21]. Moreover, differential noise compensation schemes with a sensitivity of 10^{-5} are possible using solid-state mid-IR laser sources [64] and are directly applicable to the differential scheme when the vortex and reference energies are the same at the detector. It appears thus that, for the example presented in Fig. 3(b)-3(f), the sensitivity required for the differential absorption scheme is well within actual experimental capabilities. Finally, although it exhibits a lower sensitivity than the vibrational depletion pump-probe scheme, the differential absorption approach is advantageously much simpler to implement: the careful compromise between pulse duration and spectral resolution, the need for achieving precise timing of the arrival of the pump and probe pulses at the sample, and the separation of the pump and probe beams at the detector are indeed not relevant to the differential scheme.

5. Conclusions

Simulations were used to show that simply mapping the difference in transmitted/reflected IR energy between a vortex-shaped beam and a Gaussian reference with a confocal microscope affords the generation of vibrational absorption images of spatial resolution well beyond the current state-of-the-art in IRAS far-field micro-spectroscopy. The simulations of the differential absorption reveal a spatial resolution better than $\lambda/10$ for incident energies about a decade above the saturation threshold for the CH_2 stretch in alkanes. The concept of saturated structured illumination is thus seen to be compatible with the establishment of below-the-diffraction limit, point-like PSF for measuring the IR absorbance of samples with a scanning confocal microscope set to recording the differential transmission/reflection. The detector sensitivity for organic nanoparticles is seen to be well within actual experimental capabilities.

Acknowledgments

N.H. acknowledges financial support from the CERUNA-FUNDP foundation. A.P. is a Research Director of the Belgian Fund for Scientific Research (FNRS-FRS). M.K. acknowledges funding from the Integrated Nanoscience Platform for Ireland (INSPIRE), initiated by the Higher Education Authority in Ireland within the PRTL15 framework. The LANIR research leading to these results has received funding from the European Community's Seventh Framework Programme (FP7/2012-2015) under grant agreement n°280804. This communication reflects the views only of the authors, and the Commission cannot be held responsible for any use which may be made of the information contained therein.